# Performance Evaluation of Millimeter-Wave Wearable Antennas for Electronic Travel Aid

Alicia Flórez Berdasco, Jaime Laviada, María Elena de Cos Gómez, Fernando Las-Heras

***Abstract*—The aim of this paper is to identify and evaluate the main limitations of several wearable antennas when applied to different collision avoidance situations to help visually impaired people. The analysis is conducted at a medium distance (1-2 meters, which is in the order of hundreds of wavelengths) for obstacle detection, as well as in the short distance (10-30 cm, which is in the order of tens of wavelengths) when advanced imaging techniques, based on synthetic aperture radar exploiting natural movement, are applied to generate an image of the surrounding. For this purpose, different measurements are accomplished with stepped-frequency and frequency modulated devices and subsequent error metrics are defined and applied, highlighting their main limitations for those test scenarios.**

***Index Terms*—Imaging, Electronic Travel Aid (ETA), mmWave radar, Synthetic Aperture Radar (SAR).**

## I. Introduction

WHITE CANES, sometimes supplemented by guide dogs, have been the usual resort to aid visually impaired people in their daily lives. However, it is not enough for full autonomy and safe mobility, as it does not protect against upper body collisions since it only checks the space in front of the user [1]. Consequently, many electronic travel aids (ETAs) have been developed in recent years. Most of them are based on ultrasonic sensors since these devices are low-cost [2]. Nevertheless, the main drawback of this technology is that it has difficulties to detect smooth surfaces as well as narrow apertures (e.g., semi-open doors or windows), due to its wide radiation pattern [3], [4]. Others employ infrared sensors, however these systems need direct visibility between the sensors [5]. Video cameras are another solution used as ETAs, nevertheless, they are very sensitive to natural light, which limits their resolution [1], [6] and, moreover, they do not work in low visibility environments (e.g., due to fog). There are also systems based on technologies like near-field communications (NFC) that provide high accuracy but, it can be only used for short range [5]. Therefore, most of these solutions have limitations, either in scope, precision, or even cost, encouraging a fusion of some of them [3], [7]–[11]. It is also relevant to note that ETA systems must be compact and lightweight for portability as well as comfortable. Furthermore, it is essential that the overall cost of the system must be affordable [12].

In this context, a very promising approach is the radar technology. In fact, the main key of this technology has been to detect range, angular position and speed of targets. Although it was initially developed for military purposes, nowadays there are a large number of civil applications like vehicle speed detection or astronomy ones that are based on radar technology. The principle of operation of radars is the transmission of an electromagnetic wave and the detection of the echo reflected by an object for its further processing [13]. During the last years, millimeter-wave (mmWave) radars have been widely developed by the automotive industry [14], as a result of the incorporation of advanced driver-assistance system (ADAS) in cars, which includes collision avoidance radars. Moreover, they have also been widely used at checkpoints to detect concealed weapons [15]. Besides, radar technology can operate in fog, smoke, or dust conditions.

However, in order to implement ETA solutions based on mmWave radars, the components of the system must satisfy some conditions. From the antenna point of view, it is very convenient to have flexible antennas so that they can be easy embedded in the clothing [16]–[18]. For this purpose, some flexible specific materials such as polypropylene [19] or composites [20] are recommended. In [21], the design and fabrication of a flexible screen-printed parasitic antenna array for ETA applications is shown together with its implementation and test in the complete radar system. In addition, even the complete radar system can be embedded into flexible material, as it is shown in [22], in which a wearable ETA radar system, design on semi-flexible PCB, is presented. Due to the capabilities of radars and their compactness at the mmWave band, they are very appealing to complement other ETAs technologies [23]. In particular, radar systems can operate in all environmental and lighting conditions, unlike optical sensors, that are very sensitive to natural light. Although its traditional high price has been a limitation, their massive advent due to 5G and automotive applications in the last decade, has made them affordable devices. In the case of radar systems, the resolution depends on its electrical size, which can be achieved by electrically large arrays, which is not convenient, or by means of synthetic aperture radar (SAR) techniques. The latter approach can be implemented by exploiting the natural movement of the body so that a synthetic aperture radar with high resolution can be implemented from even tiny mmWave system [24].

Thus, mmWave radar is a promising technology to be fused with some of the available technologies for ETA. In this case, it is relevant to note that the use of the antennas entails an impact, which has not been fully quantified in the literature as the impact of non-ideal radiators in this type of measurements were usually despised. Although most of the works analyzed the performance of the complete ETA system, recent studies have focused on the impact of the nonuniform amplitude of the radiation pattern [25], errors in frequency [26] or in the

positioning [27], [28]. However, the impact of the combined effect, as well as other effects such as nonuniform phase, has not been evaluated to the best authors' knowledge in final applications such as the proposed one.

In this paper, the performance of a set of antennas designed *ad hoc* for two different ETA applications based on mmWave radar (namely, short-range and medium-range applications) is analyzed taking into account the combined effects of all nonideal features of the radiation pattern (nonuniform phase/amplitude).–

Moreover, the use of wearable antennas (which can be easily embedded into garments) for the analysis, is explored for the first time to be used for both, short and medium range detection, with the challenge that this entails in terms of antenna design and manufacturing, increased by the relatively high frequency at which the system operates. On the one hand, the short-range capabilities of the antennas are evaluated by performing high-resolution imaging exploiting movement along several positions with synthetic aperture radar techniques. On the other hand, long-range applications are assessed by checking the capability to detect obstacles embedded in a multipath environment. The possibility of using the same antenna for both ranges is also taken into account.

The paper is organized as follows: first, the main concerns about obstacle detection are expose, metrics are defined and the set of antennas are presented. Next, the experimental setups for dual-purpose application (medium and short distance detection) are described and results are discussed. Finally, some conclusions are drawn.

## II. Obstacle detection with wearable mmWave antennas

In this section, the main reasons from the antenna side for inaccurate detection of targets under the medium and short distance scenarios are identified and appropriate metrics are proposed to quantified them.

### A. Concerns on obstacle detection with wearable antennas

The use of wearable mmWave radar systems for electronic travel aid has been traditionally intended for the detection of obstacles (e.g., walls, trees, etc.) at a medium distance of a few meters as farthest objects are usually not relevant [7], [29]. In addition, recent advances have shown that these systems can provide high resolution capabilities when taking advantage of the natural movement of the body as shown in [24] when working at close distances (1-2 meters, which is in the order of hundreds of wavelengths). Fig. 1 depicts both kind of applications that present a rough detection of a street lamp at medium distance and a high resolution image of the target at a closer distance. The possibility of exploiting this dual-use involves a number of concerns about the performance of the antennas, which should be flexible so that they can be easily embedded into the clothing.

Unless a system with multiple transmitter (Tx) and receiver (Rx) channels is considered (i.e., a. multiple input multiple output, MIMO, system), the detection at *medium distance* is

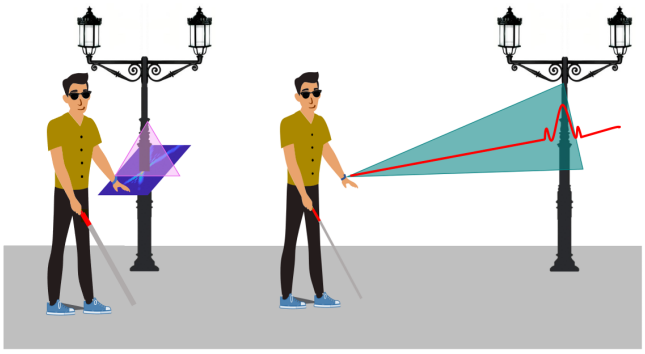

Fig. 1: Scenario of application of the prototype when a visually impaired person walks through the street for short (left) and medium (right) distance scenarios.

usually carried out by processing the range profile of the response. In the case of stepped-frequency continuous-wave (SFCW) radars as well as in the case of frequency-modulated continuous-wave (FMCW) radars, the range profile is usually found by means of an (inverse) Fourier Transform. In order to provide a good range resolution, frequency dispersive antennas should be avoided so as to not spread energy. For this purpose, the most relevant requirement is to have a linear *phase* dependency along frequency [30]. If the components and the antenna are nondispersive, the range resolution usually depends only on the bandwidth $BW$:

$$\delta_z = \frac{c}{2BW}, \tag{1}$$

wherein $c$ is the speed of light.

In the case of *short distance* as proposed in [24], the processing to build an electromagnetic image becomes slightly more complex. If the system is based on a monostatic acquisition, then the reflectivity ($\rho$) can be computed by means of a delay-and-sum algorithm

$$\rho(\overrightarrow{r}) = \sum_{m=1}^{M}\sum_{n=1}^{N} \hat{S}_{rx}(m,n)\cdot e^{jk_m 2|\vec{r}-\vec{r}_n|}, \tag{2}$$

$\vec{r}$ stands for the pixel position where reflectivity will be calculated, while $\vec{r}_n$ represents the $n$-th measured position, $k_m$ indicates the wavenumber at the $m$-th frequency and $\hat{S}_{rx}$ is the acquired $S_{rx}$ signal after the calibration explained later in this section. Finally, $M$ and $N$ are the number of frequencies and acquisition points, respectively. It is relevant to note that (2) can be implemented by means of efficient fast Fourier Transforms in order to speed up the computation [15]. When using (2), it is assumed that the antenna is creating a perfect spherical wavefront with nondispersive behavior along frequency. Under those conditions and as long as the distance to the target met the far-field requirements, the range resolution is also given by (1). The cross-range resolution is proportional to the size of the synthetic aperture as long as the beamwidth is large enough to illuminate the target from all the points of view [28]. Fig. 2 shows a schematic of the SAR imaging process.

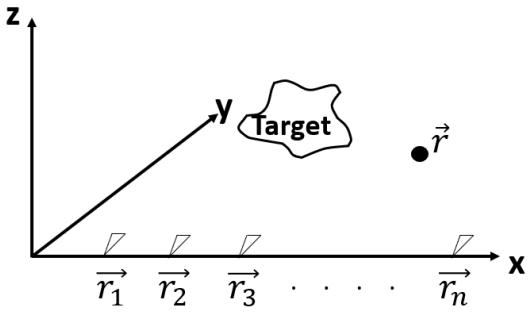


Fig. 2: Schematic of the SAR imaging process.

In order to achieve accurate images, it is important to perform a correct calibration before acquiring the data. First, the reflections of the antenna itself must be subtracted from a measurement with an empty scenario (without target) $\widetilde{S}_{rx}$. In addition, a correction has to be done at the antenna level. This correction is needed because the transmission line attached to the antenna can introduce a phase delay. However, the imaging algorithm in (2) assumes that the waves are generated at each frequency from the same position (i.e., the phase center) and with the same phase and amplitude. In practice, it is known that the linear phase offset is predominant [30] so that this adjustment is focused on correcting it. It is worth mentioning that more elaborated processing has been proposed recently to full correct the phase effects [31] at the expenses of requiring a fully vector characterization (amplitude and phase) of the antenna and including a more complex imaging algorithm. In this case, to compensate this phase dependency, the electromagnetic field is multiplied by a linear phase shift equivalent to the phase shift ($L_{eff}$). Thus, the raw data at each position and frequency are modified as follows:

$$\hat{S}_{rx}(m,n) = \left(S_{rx}(m,n) - \widetilde{S}_{rx}\right) e^{jk_m L_{eff}}. \qquad (3)$$

### B. Metrics

In the case of the medium distance testing, the metric to quantify the performance of the antenna is the amplitude of the peak corresponding to the target under test when using a multipath environment. If the antenna has a good performance, e.g., nondispersive behavior, this parameter should be correlated with the gain of the antenna under test with some uncertainty due to the multipath environment.

In the case of short distance testing, the performance is better assessed from the quality of the images, which will be obtained by applying the two following metrics. According to the application in [24], where the natural movement of the body is used, the position changes are mostly done through a single direction and, therefore, only linear SAR measurements will be considered. For the sake of simplicity, in this short distance testing, the movement will be assumed along the $x$-axis.

The target-to-noise ratio (TNR) is the first metric used to quantify the performance of the antennas. This one quantifies the energy enclosed in a given area versus the energy outside the aforementioned area. This area usually corresponds to the object or, at least, the area where the high reflectivity produced by the object is expected to be. It is defined as follows

$$TNR = 10\log_{10}\left(\frac{N_c \sum_{(x,y)\epsilon A_t} \mid \rho(x,y) \mid^2}{N_t \sum_{(x,y)\epsilon A_c} \mid \rho(x,y) \mid^2}\right), \qquad (4)$$

where $\rho$ represents the reflectivity, $A_t$ and $A_c$ stand for the areas inside and outside the target respectively. Likewise, $N_t$ denotes the number of pixels inside the desired area while $N_c$ depict the number of pixels outside the target [32] . Due to the linear movement along the $x$-axis, the only plane with resolution in both directions will be the XZ-plane as cross-range resolution is found along the $x$-axis and range resolution is found along the $z$-axis.

The second metric to be employed is the spatial resolution of an electrically small target. This resolution is defined as the distance between the first two points with half the magnitude of the maximum [27]. Since the linear movement is done only along the $x$-axis, only those cross-range resolutions are considered. However, in order to evaluate the resolution through the two main planes of the antenna, it is measured for two orthogonal rotations of the antenna (in one case the polarization of the antenna matches the y-axis while in the other the polarization agrees with the $x$-axis) (see Fig. 8) and denoted by $\delta_x$.

## III. Experimental results

In order to assess the capability of the antennas to be used with a radar in an avoidance collision system, the two aforementioned scenarios (medium and short distance situation) have been analyzed. Both measurement setups are described in detail below and the results are presented. Besides, the antennas under test with their parameters are submitted next.

Nowadays, compact commercial millimeter wave radars, based on frequency modulated (FCMW) [33], [34] and stepped frequency (SFCW) [35] technologies are available. In the case of near-field systems (e.g. human detection or non-destructive evaluation), SFCWs are preferred, while for long-range applications (e.g. driving assistance), FMCWs predominate. Since these two technologies coexist today, both FMCW and SFCW have been explored in the next sections.

### A. Antennas under test

Different wearable antennas are evaluated to be used in an avoidance collision system. For this purpose, the unlicensed frequency band 24.05-24.25 GHz is considered. On the one hand, some of these antennas utilize a conventional, though conformable, composite (RO3003 whose electrical permitivity and loss tangent are $\varepsilon_r$=3 and $\tan\delta$=0.0013, respectively, and its thickness is $h = 0.762$ mm). On the other hand,the remaining antennas use a material not originally developed for antenna design (with the difficulty involved in terms of electromagnetic characterization of the material and prototypes fabrication), polypropylene (PP), $\varepsilon_r$=2.2 and tan$\delta$=0.002

whereas its thickness is $h = 0.52\,\text{mm}$, which allows obtaining flexible and eco-friendly antennas [19].

The design of these antennas, shown in Fig. 3, can be found in [36], [37]. The set of chosen antennas includes basic patch antennas as well as small arrays. In particular, the considered antennas are a patch antenna fabricated with both previously mentioned materials (see Fig. 3a and b), two elements patch-array antenna design (see Fig. 3c) and its improved versions that include a high impedance surface (HIS) metasurface (see Fig. 3d, e and f). The HIS unit cells have been arranged between the patches to reduce the coupling, surrounding them by one row of unit cells to reduce the potential surface waves and with two rows in front of the patches to analyze the effect of the unit-cells on RO3003. In addition to the previous low-directivity antennas, a modified Dolph-Chebyshev (DC) distribution series end-fed 1x10 array antenna fabricated in both materials (see Fig. 3 g and h) is also considered to take into account an antenna with a higher gain in one of the main planes.Table I shows the radiation properties of each antenna obtained for the center frequency of the intended frequency band (24.15 GHz).

Fig. 4 shows three of the most representative measured radiation diagrams (Simple patch, two elements array and the Dolph-Chebyshev all of them on RO3003) of the antennas considered in this analysis. The rest are similar to those presented. It can be observed that, even the simple models, can significantly differ from a uniform spherical wavefront in amplitude and phase.

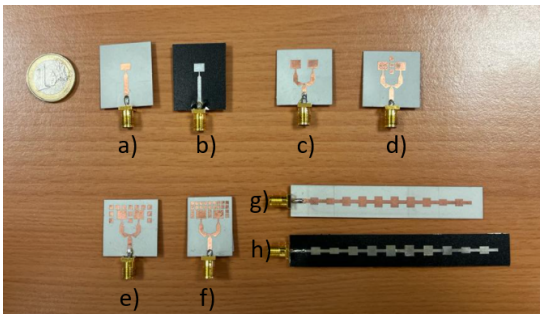


Fig. 3: Antennas under test: a) single patch on RO3003 (Patch RO), b) single patch on PP (Patch PP), c) Two elements Array on RO3003 (Basic Array), d) Two elements array with a metasurface wall on RO3003 (Wall), e) Two elements array with a single metasurface row on RO3003 (Row), f) Two-elements array with two rows of metasurface on RO3003 (2Row), g) Dolph-Chebyshev on PP (DC PP) and h) Dolph-Chebyshev on RO3003 (DC RO).

### B. Medium distance comparison

For the detection of medium distance targets, a commercial FMCW radar module has been used. Specifically, in this work the EVRADAR-MMIC2 evaluation board of Analog Devices [38], which operates in the mmWave unlicensed frequency band, from 24.05 GHz to 24.25 GHz, has been used. Although this module is not as compact as desirable for a wearable application, it has been chosen as it allows easy connection

TABLE I: Radiation properties of the antennas under test at 24.15 GHz: Gain (G), Directivity (D), efficiency ($\eta$) and front-to-back ratio (FTBR).

| | Simulation | | | | Measurement |
|---|---|---|---|---|---|
| Antenna | G (dB) | D (dB) | $\eta$ (%) | FTBR (dB) | G (dB) |
| Patch RO | 6.8 | 6.8 | 100 | 20.2 | 7.4 |
| Patch PP | 7.7 | 7.6 | 98 | 17.5 | 7.6 |
| Basic-Array | 7.3 | 7.4 | 98 | 19 | 7.4 |
| Wall | 8 | 8 | 100 | 24.8 | 8.5 |
| Row | 7.9 | 7.9 | 100 | 36.7 | 7.9 |
| 2Row | 9.2 | 9.2 | 100 | 17 | 9 |
| DC RO | 15.5 | 15.6 | 98 | 23.9 | 12.5 |
| DC PP | 16.8 | 17.2 | 91 | 25.7 | 13 |

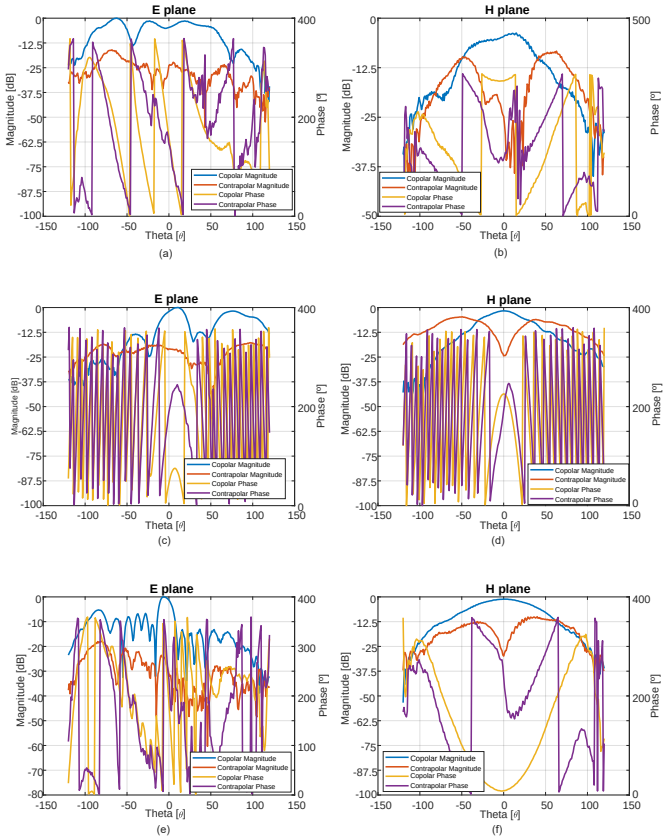


Fig. 4: Measured radiation diagrams. (a) Patch RO E plane, (b) Patch RO H plane, (c) 2Row E plane, (d) 2Row H plane, (e) DC RO E plane, (f) DC RO H plane.

of custom antennas as well as a full control of the chirp parameters (i.e., waveform, bandwidth, $BW$, and chirp time, $T_c$). In particular, a sawtooth waveform, with a bandwidth $BW$ of 200 MHz and a chirp time of $T_c = 5{\cdot}10^{-3}s$ has been used as Tx signal with an output power of 8 dBm. The output signal is the intermediate frequency (IF) signal, which is obtained from the combination of the Tx and the Rx signals.

Although the radar module allows a MIMO configuration with two transmitters and four receivers, only one transmitter and one receiver channel have been used. A separation of 20 cm has been considered in the setup. A waveguide probe (18-26.5 GHz) from MI Technologies (Model: MI-6970-WR42-K) has been employed as the Tx antenna, while the designed antennas have been used as the RX ones. The main consequence of antenna separation is an increase in

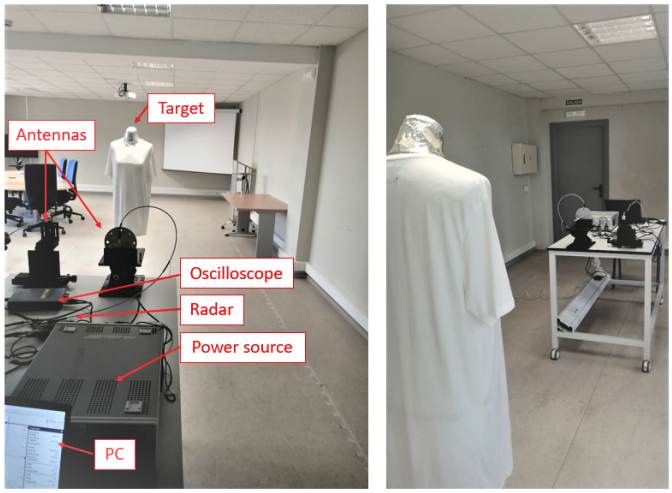


Fig. 5: Details of the measurement setup.

coupling for low beat frequencies, which can be easily filtered out, as long as it does not saturate the receiver. Regarding the multipath, for large distances to the target (meters), the separation between antennas should not have a significant impact since this kind of bistatic setup behaves as a monostatic setup for large enough distances [39].

Fig. 5 shows the measurement setup. A complex situation, similar to a final scenario, has been analyzed. In this scenario a point-target can be barely identified, due to the low reflected energy, so that a mannequin covered by aluminium foil, mimicking the skin reflectivity at mmWave frequencies has been used as target. The mannequin has been placed in a room full of furniture (tables, chairs, etc.) and different types of walls (a brick wall, plasterboard, windows, etc.), which will cause multipath. The mannequin has been situated at a distance of 1.76 m in front of the antennas and then it has been moved away until it is at a distance of 3.25 m from the antenna. The IF output signal was acquired with an oscilloscope for further processing, in order to determine if the system detects an object in front of it. The theoretical IF signal frequency has been calculated according to

$$IF = \frac{R \cdot BW}{c \cdot T_c}, \tag{5}$$

where $R$ refers to the total distance traveled by the signal, which includes the distance between the antennas and the mannequin as well as that corresponding to the cables, which were 3 m long, BW depicts the bandwidth of the Tx signal and $c$ stands for the speed of light. Fig. 6, shows the range profile by means of the IF signal, obtained with each antenna under test for both distances, 1.76 m and 3.25 m. These have been plotted together with the theoretical propagation losses $1/R^4$.

Table II summarizes the results at both distances. In the case of the target at 1.76 m, it can be observed that the main contribution is obtained around the expected distance. The slight differences are attributable to error in the compensation of the delay in the transmissions line. From these data, the range of amplitude changes 6 dB, which is in fair agreement with the

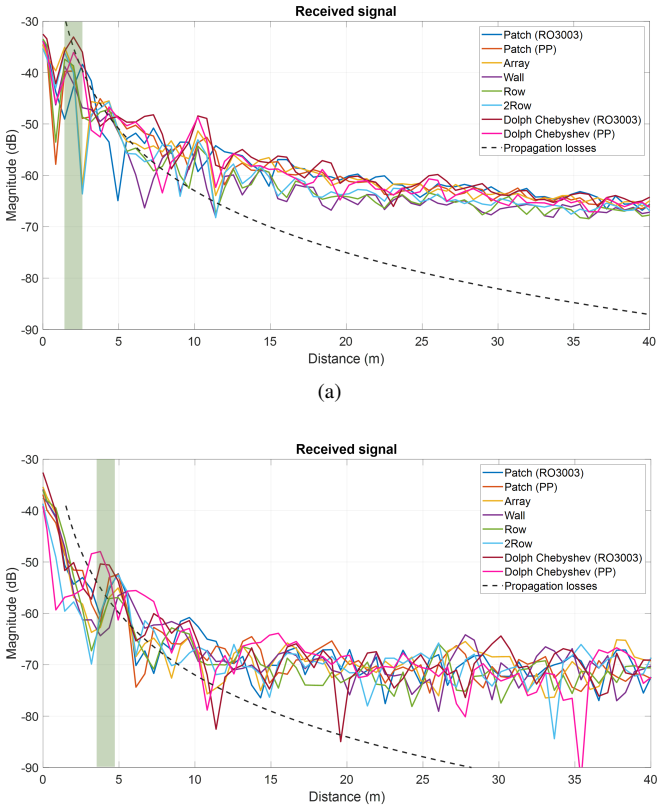


Fig. 6: IF signal for the medium distance setup. The green vertical strip shows the area where the reflections from the target are expected to be. (a) Target at a distance of 1.76m. (b) Target at a distance of 3.25m.

10 dB range of the directivity from Table I. It is interesting to note that the amplitude level does not perfectly match the gain of the antennas. These slight variations can be attributed to multipath contributions due to the wide beamwidth of the antennas. Nevertheless, it is interesting to note that the lowest value corresponds to a patch antenna whereas the greatest one corresponds to DC antennas, as it could be expected. In the case of the target at 3.25 m, the results are comparable to the previous ones, although the error in the estimation of the distance becomes larger as the distance has been increased. Nevertheless, the variation in the amplitude changes is in accordance with the previous experiment, approximately 6 dB. In addition, the highest value is obtained for a DC antenna whereas the lowest one corresponds to one of the patch-based antenna, as in the past experiment, so that the performance of the antennas is similar for both scenarios. Thus, a good agreement is found with respect to the results from Table II.

### C. Short distance comparison

In order to characterize the performance of the different antennas under test, an electrically small object is used. However, in order to increase the sensitivity, only one dimension is considered to be electrically small whereas the other one exhibits translation symmetry. The use of point-like targets is

TABLE II: Measurement results for the medium distance setups. Distance at which the target is detected (Dist), amplitude of the received contribution (Amp).

| | Target at 1.76m | | Target at 3.25m | |
|---|---|---|---|---|
| Antenna | Dist [m] | Amp [dB] | Dist [m] | Amp [dB] |
| Patch RO | 2.2 | -38.4 | 4.9 | -52.9 |
| Patch PP | 1.5 | -39.1 | 4.9 | -52.4 |
| Basic-Array | 1.5 | -35.1 | 4.9 | -55.1 |
| Wall | 1.5 | -38.8 | 5.5 | -55.7 |
| Row | 1.5 | -37.4 | 4.9 | -56.9 |
| 2 Rows | 1.5 | -36.1 | 4.9 | -52.6 |
| DC RO | 1.9 | -33.1 | 3.8 | -50.4 |
| DC PP | 1.9 | -36.1 | 3.8 | -47.9 |

quite common when evaluating near-field imaging system, as this kind of objects provide a simple response and artifacts can be easily identify, so that the analysis of the results is easier [27], [28]. Specifically, a metal strip with dimensions of 4 mm×340 mm is used. This strip is placed at a distance of 13.2 cm over the antenna (see Fig. 7). In order to avoid any uncertainty due to the cable movement, the antenna under test remains static and the target is moved by means of a motorized linear micropositioner.

In this case, a pure monostatic setup has been used, so that a single antenna is used as transmitter and receiver. Although it reduces the sensitivity due to the own antenna reflections, it is preferred, as it avoids including the effects of a second radiation pattern. Hence, most potential errors in the results are caused by the radiation pattern of the measurement antenna and by measurement uncertainties. The antenna under test has been placed under the object and a VNA has been used to measure the scattering parameter $S_{11}$, emulating a SFCW radar.

It is necessary to highlight that, in the case of the wrist-mounted device, as illustrated in [24], the tracking of the position based on accelerometers tends to accumulate a significant error and, therefore, only relative positions in a short period of time are coherent. However, even so, a large gain is obtained when combining the contributions at the corresponding positions obtained for a short-period of time. Thus, the results obtained for a linear movement (1 axis) are expected to be a fair estimation of a fraction of a pendulum-like motion. Hence, in this work the relative movement of metal strip along a path of 30 cm in the direction of the $x$-axis is considered.

Moreover, no significant Doppler effect is expected as synthetic aperture radar techniques are applied to the volume in front of the synthetic aperture and not in the direction in which the antenna in moved, so that the Doppler effect only takes place in the radial direction. This has been empirically illustrated for freehand imaging in [40] wherein the movement is parallel to the target plane.

Measurement data have been acquired with a step of 4 mm ($\sim\lambda/4$ at the highest frequency) to satisfy the sampling conditions of the Nyquist theorem. In this case, uniform sampling by means of a motorized micropositioner has been chosen in order to employ the same benchmark for all the antennas and avoid artifacts from irregular sampling so all the undesired effects are due to the nonideal radiation pattern. A laser level was used to align the antenna under test with the center of the synthetic aperture and the midpoint of the metal strip.

TABLE III: Experimental parameters established for short distance evaluation.

| | |
|---|---|
| Center Frequency [GHz] | 24.15 |
| Bandwitdh [MHz] | 200 |
| Number of frequencies used | 161 |
| IF bandwidth [kHz] | 100 |
| Synthetic Aperture Length [cm] | 30 |
| Sampling Step [mm] | 4 |
| Target Dimensions [mm] | 340x4 |

Table III summarizes the experimental parameters set for the short distance evaluation.

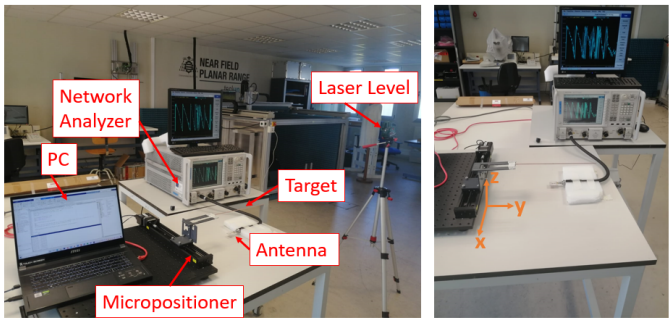


Fig. 7: Measurement Setup 2.

A calibration has been performed to remove systematic errors produced by cables, transitions, etc. so that the $S_{11}$ parameter is measured at the connector of the antenna. After that, the correction given by (3) is carried out.

In order to find the optimum $L_{eff}$, a sweep has been accomplished until the object appears in the image at its original position (i.e., 13.2 cm). The estimated value of $L_{eff}$ for each antenna is shown in Table IV.

In order to characterize the short distance detection performance of the antennas for each main plane, two sets of linear measurements have been performed. In the first one, the polarization of the antenna matches with the $y$-axis, while in the second one, the antennas has been rotated and the polarization agrees with the $x$-axis.

Using (2), electromagnetic images have been obtained at the intended frequency band. Fig. 9 shows the electromagnetic images at XY and XZ planes respectively, when the antenna

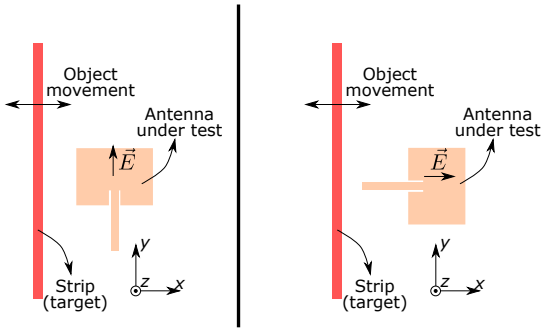


Fig. 8: Measurement setups for the two sets of measurements in the short distance comparison.

is polarized along the $y$-axis and the strip is also parallel to that axis. In addition, the strip is moved along a line perpendicular to the polarization direction ($x$-axis). Due to the linear movement along the $x$-axis, the detected object only shows resolution in the $x$-direction. The width along this axis, is denoted by $\delta_x$ in Table IV. As expected, for this set of measurements, there is no resolution along the $y$-direction so it is not considered here. In addition, images on the XZ plane have also been calculated. In this case, the (range) resolution along the $z$-axis is typically better than the theoretical resolution given by (1) [15]. This is due to the very near-field of the synthetic aperture (the size of the aperture, 30 cm, is significantly larger that the distance to the target 13.2 cm) and, even, simulations with an ideal nondispersive and isotropic antenna show this super-resolution along range (see Fig. 10) for the theoretical image when using a perfectly isotropic antenna.

The same phenomena occurs for the second set of measurements after rotating the antenna. Thus, resolution is found only along the $x$-axis but not along the $y$-axis and, again, the range resolution (i.e., along the $z$-axis) is still better than the one given by (1) as can be seen in Fig. 9.

The metrics from the previous section are applied independently for each set of measurements to check the performance of the antenna in both axis.

In order to quantify the TNR, an investigation domain (mask) has been established in order to delimit the target

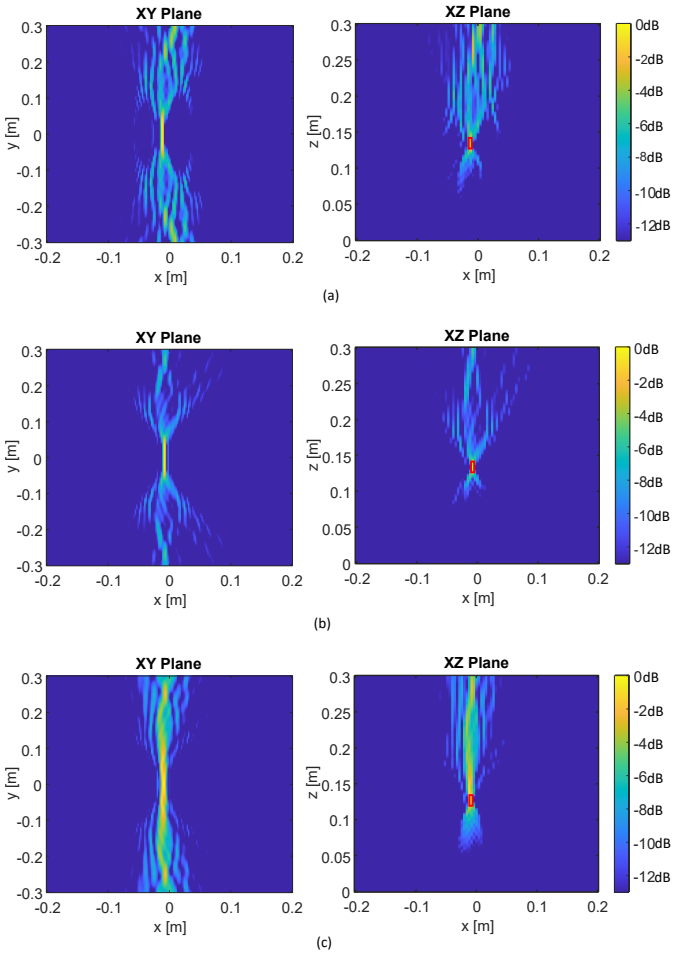


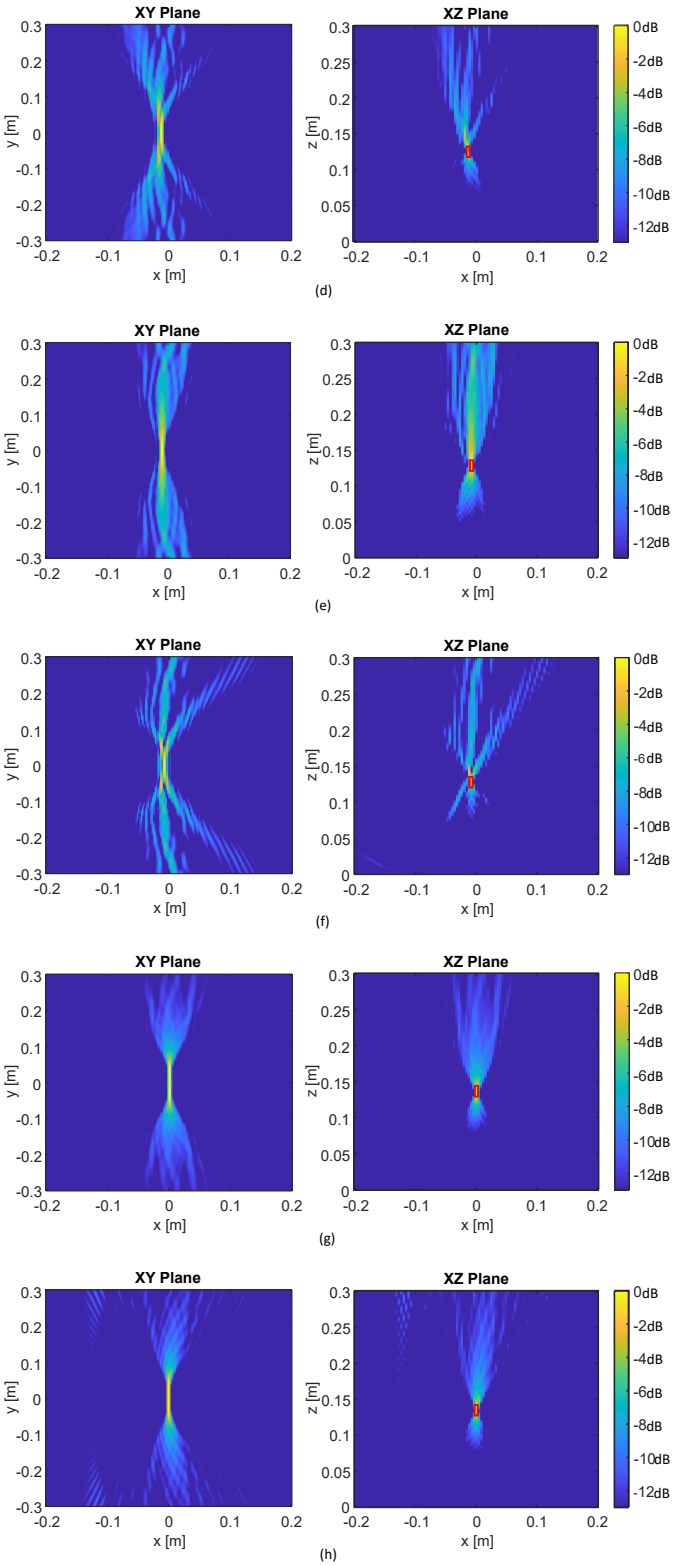


Fig. 9: Electromagnetic images obtained with each antenna for the $y$-polarization: (a) Patch RO3003, (b) Patch PP, (c) Basic Array, (d) Wall, (e) Row, (f) 2Row, (g) DC RO3003 and (h) DC PP.

as it could be seen in color red in Fig. 9 for the $y$-polarization. The width of the mask (coinciding with the $x$-axis) has been established according to the real size of the

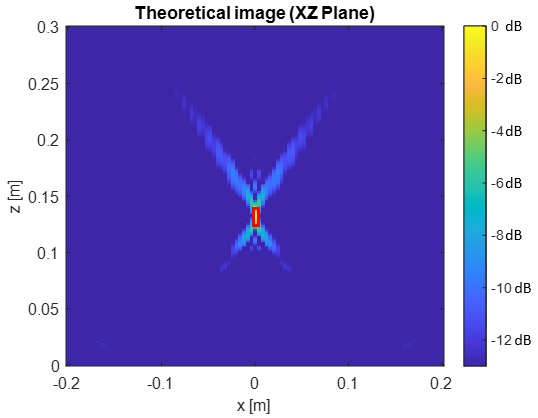


Fig. 10: Theoretical image obtained with an ideal nondispersive and isotropic antenna.

metal strip (4 mm), while the length (coinciding with the $y$-axis) has been set from the theoretical image obtained with an ideal nondispersive and isotropic antenna in the same conditions as the measurement as shown in Fig. 10. Specifically, to establish the length, the pixels that have a reflectivity level greater than $-3$ dB have been taken into account.

The results are summarized in Table IV. Attending to the TNR results, it can be seen that the best ones are obtained for the antenna polarization situated along the $y$-axis for most of the antennas. However, if the antenna is rotated and its polarization is matched with the $x$-axis, the results are degraded for the great part of the antennas under test. This is expected as currents are better induced when the polarization of the incident field is parallel to the strip, since the boundary condition sets the electric current perpendicular to the edges to be zero.

The result of the DC antennas, which obtain the lowest TNR, is especially noteworthy. It happens when the antenna polarization is placed along the $x$-axis, since the DC antennas are much longer along the scanning direction and, therefore, the spherical wavefront expected by (2) is not met at all.

In fact, the strip is so close that not the entire antenna but only the closest patches are expected to contribute to the transmission and reception. In the other position of the antenna, this effect is not as strong as the antenna is narrower and the field is expected to match better a spherical-wave. Apart from that exception, the TNR values are similar for all the antennas, especially when it is placed along $y$-axis, which indicates that all of them are suitable for the imaging at close distances.

The linear cuts used for the resolution calculation are shown in Fig. 11.

Regarding the spatial resolution, as shown in Table IV, in case of considering the antenna with polarization along the $y$-axis, the spatial resolution, denoted by $\delta_x^{(y-pol)}$, is practically the same for all the antennas, which reveals that the resolution is not limited by the beamwidth of the antennas but by the length of synthetic aperture.

Nevertheless, if the antenna is polarized along the $x$-axis (resolution denoted by $\delta_x^{(x-pol)}$), larger differences in spatial resolution can be observed, especially in the case of the DC PP antenna. As explained above, this is because it is an electrically larger and more complex antenna so the field does not behave yet as a spherical wave, and therefore, the object appears with a larger trail.

Consequently small antennas (1-2 electrically small elements) have a better performance at short distances even if their gain is lower.

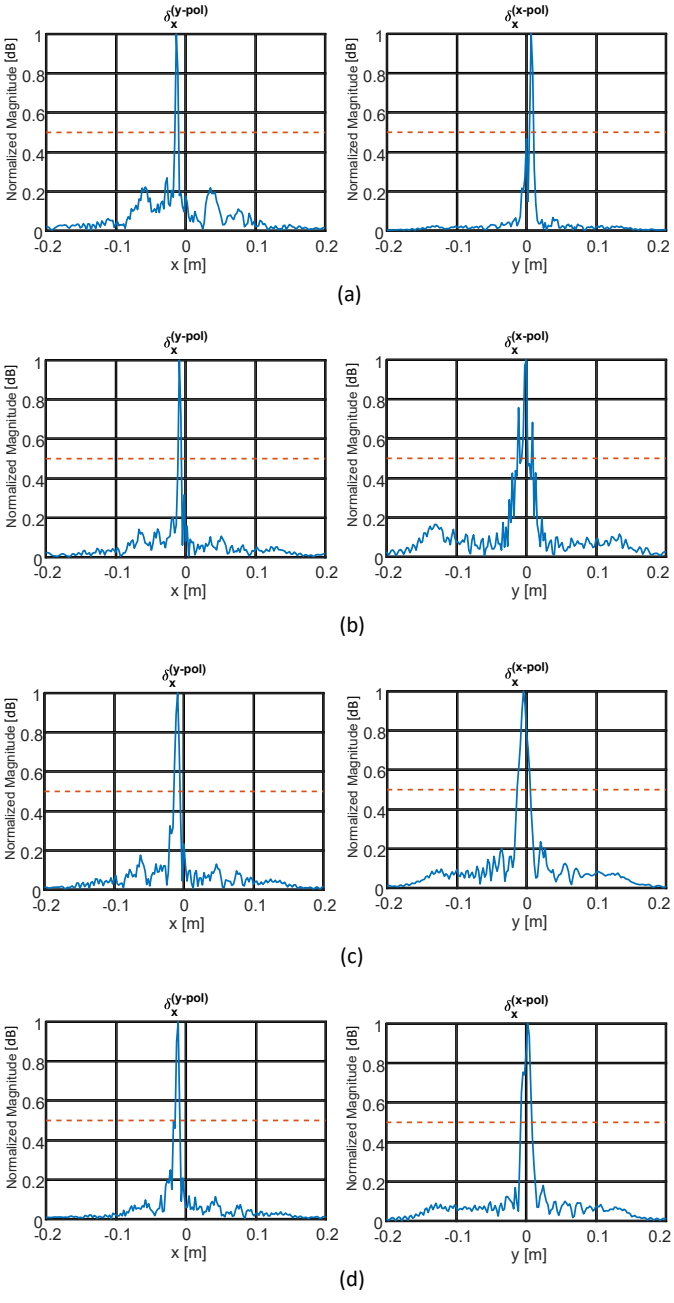

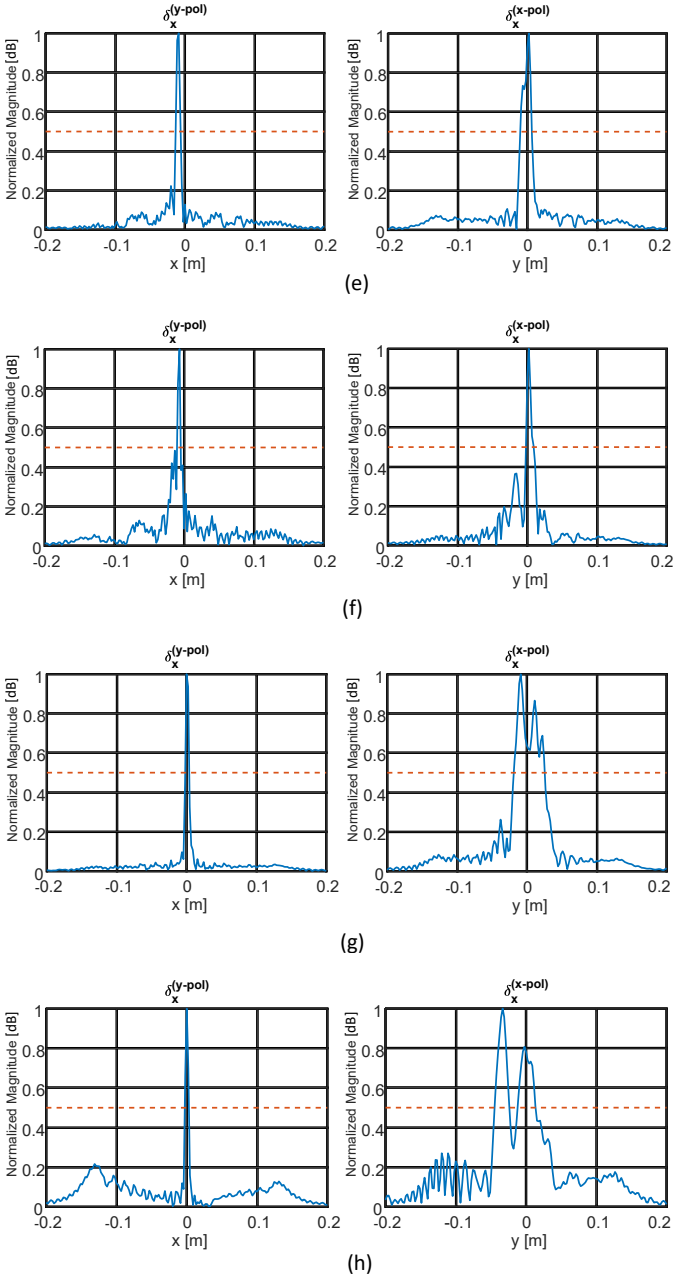


Fig. 11: Spatial resolution: (a) Patch RO3003, (b) Patch PP, (c) Basic Array, (d) Wall, (e) Row, (f) 2Row, (g) DC RO3003 and (h) DC PP.

TABLE IV: Measurement results of the short distance comparison.

| | | Antenna polarized according to $y$-axis | | Antenna polarized according to $x$-axis | |
|---|---|---|---|---|---|
| Antenna | $L_{eff}$[mm] | $\delta_x^{(y-pol)}[mm]$ | TNR [dB] (XZ plane) | $\delta_x^{(x-pol)}$ [mm] | TNR [dB] (XZ plane) |
| Patch RO | 0.12 | 5.4 | 13.7 | 6.1 | 15.4 |
| Patch PP | 0.1 | 5 | 14.2 | 22.4 | 9.3 |
| Basic Array | 0.11 | 8.9 | 14.1 | 15.7 | 13.6 |
| Wall | 0.11 | 6.6 | 15.1 | 16 | 13.8 |
| 1 Row | 0.11 | 7.2 | 14.8 | 17.6 | 14.2 |
| 2 Row | 0.105 | 5.4 | 13.1 | 15.8 | 14.2 |
| DC RO | 0.29 | 5.8 | 15.8 | 44 | 10.5 |
| DC PP | 0.3 | 5.9 | 14.4 | 52 | 10.8 |

## IV. Conclusions

Nonideal performance of antennas in terms of angular amplitude and phase changes as well as non ideal correction of frequency phase shift can have an impact in the performance of imaging systems. This performance has been evaluated in the case of wearable mmWave antennas for ETA systems. In particular, the detection at medium and short distances, using direct processing as well as imaging based on synthetic aperture radar, has been considered. In the case of medium distance detection, the results are, as expected, mostly correlated with the gain of the antennas. Nevertheless, in the case of the short distance detection (10- 30 cm, which is in the order of tens of wavelengths) when, the antennas show different performance in terms of energy spread and resolution. Antennas with low directivity (one or two patches) can accomplish a good performance without relevant differences between them. If the gain is larger, and so the electrical size of the antenna, special care must be paid as anomalous results are expected along the electrically large dimension of the antenna. Consequently, ETA systems with dual performance (i.e., short and medium distances) are expected to behave better with low gain antennas whereas systems targeting only medium distance detection perform better with higher gain antennas.

## Acknowledgment

Funded by the Ministerio de Ciencia e Innovación of Spain under the FPI Grant MCIU-20-PRE2019-089912 and project META-IMAGER PID2021-122697OB-I00, and by Gobierno del Principado de Asturias under project AYUD-2021-51706.

## References

[1] L. Scalise et al., "Experimental Investigation of Electromagnetic Obstacle Detection for Visually Impaired Users: A Comparison With Ultrasonic Sensing,", *IEEE Transactions on Instrumentation and Measurement*, vol. 61, no. 11, pp. 3047-3057, Nov. 2012, doi: 10.1109/TIM.2012.2202169.

[2] D. Abreu, J. Toledo, B. Codina and A. Suárez, "Low-Cost Ultrasonic Range Improvements for an Assistive Device," *Sensors* vol. 21,12 4250, 21 Jun. 2021, doi: 10.3390/s21124250.

[3] E. Cardillo, C. Li and A. Caddemi, "Millimeter-Wave Radar Cane: A Blind People Aid With Moving Human Recognition Capabilities," *IEEE Journal of Electromagnetics, Rf and Microwaves in Medicine and Biology*, vol. 6, no. 2, pp. 204-211, June 2022, doi: 10.1109/JERM.2021.3117129.

[4] E. Cardillo, A. Caddemi, "Insight on Electronic Travel Aids for Visually Impaired People: A Review on the Electromagnetic Technology," *Electronics 2019,* vol. 8, no. 8, 2019, doi:10.3390/electronics8111281.

[5] D. Plikynas, A. Žvironas, M. Gudauskis, A. Budrionis, P. Daniušis and I. Sliesoraitytė, "Research advances of indoor navigation for blind people: A brief review of technological instrumentation," in IEEE Instrumentation & Measurement Magazine, vol. 23, no. 4, pp. 22-32, June 2020, doi: 10.1109/MIM.2020.9126068.

[6] A. Zvironas, M. Gudauskis and D. Plikynas, "Indoor Electronic Traveling Aids for Visually Impaired: Systemic Review," *2019 International Conference on Computational Science and Computational Intelligence (CSCI)*, 2019, pp. 936-942, doi: 10.1109/CSCI49370.2019.00178.

[7] N. Long, H. Yan, L. Wang, H. Li, Q. Yang, "Unifying Obstacle Detection, Recognition, and Fusion Based on the Polarization Color Stereo Camera and LiDAR for the ADAS". Sensors 2022, 22, 2453. https://doi.org/10.3390/s22072453.

[8] K. Wang, R. Cheng, K. Yang, J. Bai, and N. Long, "Fusion of millimeter wave radar and RGB-depth sensors for assisted navigation of the visually impaired," Proc. SPIE, vol. 10800, Oct. 2018, Art. no. 1080006, doi: 10.1117/12.2324626.

[9] N. Long, K. Wang, R. Cheng, W. Hu, K. Yang. "Unifying obstacle detection, recognition, and fusion based on millimeter wave radar and RGB-depth sensors for the visually impaired," *Rev Sci Instrum*, 2019 Apr, 90(4):044102, doi: 10.1063/1.5093279. PMID: 31042998.

[10] S.Pisa, E. Pittella, E. Piuzzi, "Serial patch array antenna for an FMCW radar housed in a white cane," *Int. J. Antennas Propag*, 2016, 2016, 9458609, doi: 10.1155/2016/9458609.

[11] V. Di Mattia et al., "A feasibility study of a compact radar system for autonomous walking of blind people," *2016 IEEE 2nd International Forum on Research and Technologies for Society and Industry Leveraging a better tomorrow (RTSI)*, 2016, pp. 1-5, doi: 10.1109/RTSI.2016.7740599.

[12] A. Kumar, R. Patra, M. Manjunatha, J. Mukhopadhyay and A. K. Majumdar, "An electronic travel aid for navigation of visually impaired persons," *2011 Third International Conference on Communication Systems and Networks (COMSNETS 2011)*, 2011, pp. 1-5, doi: 10.1109/COMSNETS.2011.5716517.

[13] I. M. Skolnik, Introduction to RADAR Systems, New York, NY, USA: McGraw-Hill, 1980.

[14] S. M. Patole, M. Torlak, D. Wang and M. Ali, "Automotive radars: A review of signal processing techniques," *IEEE Signal Processing Magazine*, vol. 34, no. 2, pp. 22-35, March 2017, doi: 10.1109/MSP.2016.2628914.

[15] D. M. Sheen, D. L. McMakin and T. E. Hall, "Three-dimensional millimeter-wave imaging for concealed weapon detection," *IEEE Transactions on Microwave Theory and Techniques*, vol. 49, no. 9, pp. 1581-1592, Sept. 2001, doi: 10.1109/22.942570.

[16] M. Wagih, A. S. Weddell and S. Beeby, "Millimeter-Wave Textile Antenna for on-Body RF Energy Harvesting in Future 5G Networks," *2019 IEEE Wireless Power Transfer Conference (WPTC)*, 2019, pp. 245-248, doi: 10.1109/WPTC45513.2019.9055541.

[17] M. Cupal and Z. Raida, "Circularly polarized substrate integrated textile antenna for ISM band 24 GHz," *2017 International Conference on Electromagnetics in Advanced Applications (ICEAA)*, pp. 1154-1157, 2017. https://doi.org/10.1109/ICEAA.2017.8065472.

[18] M. E. de Cos Gómez, H. Fernández Álvarez, A. Flórez Berdasco , F. Las-Heras Andrés, "Paving the Way to Eco-Friendly IoT Antennas: Tencel-Based Ultra-Thin Compact Monopole and Its Applications to ZigBee," *Sensors (Basel)*, 2020 Jun 30;20(13):3658, doi: 10.3390/s20133658.

[19] M. E. de Cos and F. Las-Heras, "Polypropylene-Based Dual-Band CPW-Fed Monopole Antenna," *IEEE Antennas and Propagation Magazine*, vol. 55, no. 3, pp. 264-273, June 2013, doi: 10.1109/MAP.2013.6586683.

[20] M.E de Cos Gómez, H. Fernández Álvarez, B. Puerto Valcarce, C. García González, J. Olenick, F. Las-Heras Andrés, "Zirconia-Based Ultra-Thin Compact Flexible CPW-Fed Slot Antenna for IoT," *Sensors 2019*, 19, 3134. https://doi.org/10.3390/s19143134.

[21] A. Meredov, K. Klionovski and A. Shamim, "Screen-Printed, Flexible, Parasitic Beam-Switching Millimeter-Wave Antenna Array for Wearable Applications," in IEEE Open Journal of Antennas and Propagation, vol. 1, pp. 2-10, 2020, doi: 10.1109/OJAP.2019.2955507.

[22] Z. Haoran, Y. Yiming, Z. Jiahao, S. Atif, "Wearable Radar System Design on Semi-Flexible PCB for Visually Impaired People", *Frontiers in Communications and Networks*, vol.2, 2022, doi: 10.3389/frcmn.2021.768794.

[23] T. Kiuru et al, "Assistive device for orientation and mobility of the visually impaired based on millimeter wave radar technology—Clinical investigation results," *Cogent Engineering*, Vol. 5, 2018.

[24] H. F. Álvarez, G. Álvarez-Narciandi, F. Las-Heras and J. Laviada, "System Based on Compact mmWave Radar and Natural Body Movement for Assisting Visually Impaired People," *IEEE Access*, vol. 9, pp. 125042-125051, 2021, doi: 10.1109/ACCESS.2021.3110582.

[25] C. Liu, M. T. A. Qaseer and R. Zoughi, "Influence of Antenna Pattern on Synthetic Aperture Radar Resolution for NDE Applications," *IEEE Transactions on Instrumentation and Measurement*, vol. 70, pp. 1-11, 2021, Art no. 8000911, doi: 10.1109/TIM.2020.3026122.

[26] M. J. Horst, M. T. Ghasr and R. Zoughi, "Effect of Instrument Frequency Uncertainty on Wideband Microwave Synthetic Aperture Radar Images," in IEEE Transactions on Instrumentation and Measurement, vol. 68, no. 1, pp. 151-159, Jan. 2019, doi: 10.1109/TIM.2018.2834098

[27] Y. Gao, M. T. Ghasr and R. Zoughi, "Effects of translational position error on microwave synthetic aperture radar (SAR) imaging systems," *2018 IEEE International Instrumentation and Measurement Technology Conference (I2MTC)*, 2018, pp. 1-6, doi: 10.1109/I2MTC.2018.8409556.

[28] Y. Gao, M. T. Ghasr and R. Zoughi, "Effects of and Compensation for Translational Position Error in Microwave Synthetic Aperture Radar Imaging Systems," *IEEE Transactions on Instrumentation and Measurement*, vol. 69, no. 4, pp. 1205-1212, April 2020, doi: 10.1109/TIM.2019.2910340.

[29] E. Cardillo, V. Di Mattia, G. Manfredi, P. Russo, A. De Leo, A. Caddemi, and G. Cerri, "An electromagnetic sensor prototype to assist visually impaired and blind people in autonomous walking," *IEEE Sensors J.*, vol. 18, no. 6, pp. 2568–2576, Mar. 2018, doi: 10.1109/JSEN.2018.2795046.

[30] X. Tian, Q. Guo, Z. Wang, T. Chang and H. -L. Cui, "Pragmatic Approach to Phase Self-Calibration for Planar Array Millimeter-Wave MIMO Imaging," *IEEE Transactions on Instrumentation and Measurement*, vol. 70, pp. 1-11, 2021, Art no. 4501111, doi: 10.1109/TIM.2020.3031167.

[31] Y. Á. López and F. Las-Heras, "On the Use of an Equivalent Currents-Based Technique to Improve Electromagnetic Imaging," in IEEE Transactions on Instrumentation and Measurement, vol. 71, pp. 1-13, 2022, Art no. 8004113, doi: 10.1109/TIM.2022.3181926.

[32] L. Liu, Q. Chen, Y. Han, H. Xu, J. Li and B. Wang, "Improved Clutter Removal by Robust Principal Component Analysis for Chaos Through-Wall Imaging Radar," *Electronics* 2020, 9, 25, doi: 10.3390/electronics9010025.

[33] Lien, J., Gillian, N., Karagozler, M., Amihood, P., Schwesig, C., Olson, E., Raja, H., Poupyrev, I. 2016. Soli: Ubiquitous Gesture Sensing with Millimeter Wave Radar. ACM Trans. Graph. 35, 4, Article 142 (July 2016), 19 pages. DOI = 10.1145/2897824.2925953 http://doi.acm.org/10.1145/2897824.2925953.

[34] Xing, S.; Song, S.; Quan, S.; Sun, D.; Wang, J.; Li, Y. Near-Field 3D Sparse SAR Direct Imaging with Irregular Samples. Remote Sens. 2022, 14, 6321. https://doi.org/10.3390/ rs14246321

[35] E. Sirignano, A. Davoli, G. M. Vitetta and F. Viappiani, "A Comparative Analysis of Deterministic Detection and Estimation Techniques for MIMO SFCW Radars," in IEEE Access, vol. 7, pp. 129848-129861, 2019, doi: 10.1109/ACCESS.2019.2939432.

[36] A. F. Berdasco, M. E. de Cos Gómez, H. F. Álvarez and F. L. -H. Andrés, "Array Antenna with HIS Metasurface for mmWave Imaging Applications," *2022 16th European Conference on Antennas and Propagation (EuCAP)*, 2022, pp. 1-5, doi: 10.23919/EuCAP53622.2022.9769433.

[37] M. E. de Cos Gómez, H. F. Álvarez and F. L. -H. Andrés, "Millimeter Wave Antenna on Eco-friendly Substrate for Radar Applications," *2022 16th European Conference on Antennas and Propagation (EuCAP)*, 2022, pp. 1-5, doi: 10.23919/EuCAP53622.2022.9769364.

[38] EVRADAR-MMIC2 evaluation board of Analog Devices [Online]. Available: https://www.analog.com/en/design-center/evaluation-hardware-and-software/evaluation-boards-kits/eval-radar-mmic.html

[39] J. W. Smith and M. Torlak, "Efficient 3-D Near-Field MIMO-SAR Imaging for Irregular Scanning Geometries," in IEEE Access, vol. 10, pp. 10283-10294, 2022, doi: 10.1109/ACCESS.2022.3145370.

[40] G. Álvarez-Narciandi, M. López-Portugués, F. Las-Heras and J. Laviada, "Freehand, Agile, and High-Resolution Imaging With Compact mm-Wave Radar," in IEEE Access, vol. 7, pp. 95516-95526, 2019, doi: 10.1109/ACCESS.2019.2929522.